How to cite: *Angew. Chem. Int. Ed.* **2022,** *61,* e202209268
International Edition: doi.org/10.1002/anie.202209268
German Edition: doi.org/10.1002/ange.202209268

CO_2 Reduction Reaction

Over 70 % Faradaic Efficiency for CO_2 Electroreduction to Ethanol Enabled by Potassium Dopant-Tuned Interaction between Copper Sites and Intermediates

Lianchun Ding, Nannan Zhu, Yan Hu, Zheng Chen, Pin Song, Tian Sheng, Zhengcui Wu,* and Yujie Xiong**

Abstract: It is highly desired yet challenging to steer the CO_2 electroreduction reaction (CO_2ER) toward ethanol with high selectivity, for which the evolution of reaction intermediates on catalytically active sites holds the key. Herein, we report that K doping in Cu_2Se nanosheets array on Cu foam serves as a versatile way to tune the interaction between Cu sites and reaction intermediates in CO_2ER, enabling highly selective production of ethanol. As revealed by characterization and simulation, the electron transfer from K to Se can stabilize Cu^I species which facilitate the adsorption of linear $*CO_L$ and bridge $*CO_B$ intermediates to promote C–C coupling during CO_2ER. As a result, the optimized $K_{11.2\%}$-Cu_2Se nanosheets array can catalyze CO_2ER to ethanol as a single liquid product with high selectivity in a potential area from −0.6 to −1.2 V. Notably, it offers a Faradaic efficiency of 70.3 % for ethanol production at −0.8 V with as is stable for 130 h.

Introduction

The CO_2 electroreduction reaction (CO_2ER) to valuable products offers a sustainable way for a carbon-neutral cycle to lessen the emission of greenhouse gases. Among various CO_2ER products, C_{2+} products have received tremendous attention due to their high energy density and economic value compared to C_1 products. Ethanol, as a liquid oxygenate C_2 product with easy storage and transport, has been widely used as a solvent and raw material to produce organic chemicals and disinfectants. However, it remains a challenge to develop the catalysts that can efficiently electrocatalyze CO_2 to C_{2+} products due to the low controllability over C–C coupling. Even with successful C–C coupling, such a reaction system is still hindered by the dominant production of ethylene, which has been commonly observed in CO_2ER, due to its low activation energy barrier relative to other C_{2+} products.[1] The control of the evolution of the reaction intermediates is the key to overcome this limitation and relies on the catalyst design.[2]

Metallic Cu is an effective catalyst for CO_2ER to multicarbon products but is typically limited by low activity and selectivity due to its high surface mobility and low cohesive energy.[3] To this end, various strategies, such as coating with nitrogen-doped carbon layers, functionalization with metal complexes, and use of copper compound catalysts, have been developed to maneuver reaction intermediates at catalytically active sites, enabling ethanol production from CO_2ER with Faradaic efficiencies (FEs) up to 52 %.[4–7] These approaches have provided important insights for further development of Cu-based catalysts toward ethanol production, which indicate both the valence state and subsurface electronic structure of catalytically active sites can serve as ways to tune CO_2ER performance. For instance, it has been revealed that the active Cu^I species confined in Cu_2O nanocavities can facilitate multicarbon alcohol production by tuning reaction intermediates during CO_2ER process.[6] In parallel, it has been reported that chalcogen atoms in the subsurface of Cu-based catalysts can alter the electronic structures of catalytically active sites to promote multicarbon alcohol formation.[7] As such, a conception naturally comes up whether copper chalcogenides, which have higher electrical conductivities than the commonly used copper oxide catalysts, can be implemented as catalysts for CO_2ER to ethanol. As a matter of fact, various copper chalcogenides have been applied in CO_2ER; however, despite the tunable catalytic activity by composition control, most of them are still limited to yield C_1 products under ambient conditions.[8,9] This circumstance should be closely related to the thorough reduction of Cu sites to Cu^0 species during CO_2ER, limiting the adsorption and dimerization of *CO intermediates.

[*] L. Ding, N. Zhu, Y. Hu, Prof. Z. Chen, Prof. P. Song, Prof. T. Sheng, Prof. Z. Wu, Prof. Y. Xiong
Key Laboratory of Functional Molecular Solids, Ministry of Education, Anhui Key Laboratory of Molecule-Based Materials, Anhui Provincial Engineering Laboratory of New-Energy Vehicle Battery Energy-Storage Materials, Anhui Engineering Research Center of Carbon Neutrality, College of Chemistry and Materials Science, Anhui Normal University
Wuhu 241002 (P. R. China)
E-mail: tsheng@ahnu.edu.cn
zhengcui@ahnu.edu.cn
Prof. Y. Xiong
School of Chemistry and Materials Science, Hefei National Research Center for Physical Sciences at the Microscale, University of Science and Technology of China
Hefei 230026 (P. R. China)
E-mail: yjxiong@ustc.edu.cn

Herein, we demonstrate that the doping of K^+ cations into Cu_2Se nanosheets array can retain Cu^I sites during CO_2ER to maneuver reaction intermediates toward highly selective ethanol production. Our characterizations reveal that such active site engineering via K doping increases the binding strength of $*CO_B$ and $*CO_L$ on the catalyst surface, promoting subsequent C–C coupling to produce ethanol. Furthermore, density functional theory (DFT) calculation indicates that K-doped Cu_2Se with exposed (110) planes energetically prefers the generation of ethanol rather than other carbon products such as CO, methanol, methane and ethylene, and also prevents competitive hydrogen evolution reaction (HER) during CO_2ER. As a result, the optimized $K_{11.2\%}$-Cu_2Se nanosheets array can catalyze CO_2ER to ethanol as a single liquid product, with a Faradaic efficiency as high as 70.3 % and a partial current density reaching 35.8 mA cm^{-2} at −0.8 V in 0.1 M $KHCO_3$ with an extraordinary stability for 130 h. Encouragingly, the Faradaic efficiency of ethanol on $K_{11.2\%}$-Cu_2Se is above 50 % in a broad potential area from −0.6 to −1.2 V. This work puts forward a strategy for dramatically enhanced CO_2ER to ethanol, through doping alkali metal cations into Cu chalcogenides to control the key reaction intermediate evolution.

Results and Discussion

The synthesis of K-doped Cu_2Se nanosheets array on Cu foam is achieved through a one-step solution-phase method. As revealed by scanning electron microscopy (SEM) and transmission electron microscopy (TEM), the obtained $K_{11.2\%}$-Cu_2Se possesses an interconnected honeycomb-like array structure composed of nanosheets, where the nanosheets have the lateral size of ≈320 nm with flexibility (Figure 1a–c). In comparison, the undoped Cu_2Se comprises of similar nanosheets with slightly larger size of ≈340 nm (Figure S1). Such $K_{11.2\%}$-Cu_2Se and Cu_2Se nanosheets arrays form a layer with approximate thickness of 1.4 and 1.8 μm on Cu foam, respectively (Figure S2). The $K_{11.2\%}$-Cu_2Se nanosheets are further examined by high-resolution TEM (HRTEM), which shows the interplanar spacing of 0.205 nm corresponding to (220) facet of cubic Cu_2Se (Figure 1d). The existence of K in $K_{11.2\%}$-Cu_2Se is manifested by energy-dispersive X-ray (EDX) spectroscopy (Figure 1e), indicating that the K content is approximately 11.2 % in addition to the stoichiometric composition of Cu_2Se. Further SEM elemental mapping shows that Cu, Se and K elements are uniformly dispersed in $K_{11.2\%}$-Cu_2Se, in which the density of K element is relatively low (Figure 1f). To evaluate the effect of K content on CO_2ER, two control examples with K doping content of 5.9 % and 15.9 % are prepared to have similar nanosheets array structures with lateral sizes of ≈300 and ≈410 nm, respectively (Figure S3). X-ray diffraction further confirms that the nanosheets maintain the crystal phase of cubic Cu_2Se (JCPDS no: 65-2982) but exhibit the increase of lattice parameters from 5.761 Å to 5.803 Å along with the replacement of Cu^+ cations by a small number of K^+ cations, and Raman spectroscopy identifies that such a replacement makes the change to Cu–Se bonds (Figure S4).

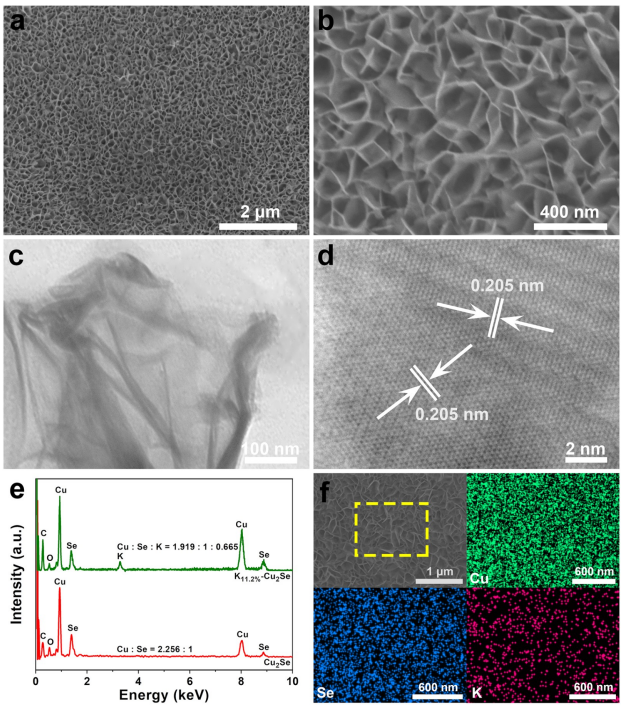

Figure 1. a), b) SEM images, c) TEM image and d) HRTEM image of $K_{11.2\%}$-Cu_2Se. e) EDX spectra of $K_{11.2\%}$-Cu_2Se and Cu_2Se. f) SEM elemental mapping images of $K_{11.2\%}$-Cu_2Se.

Our DFT calculations further demonstrate that the replacement of Cu^+ cations by K^+ cations causes the increase of Cu–Se bond length from 2.516 Å to 2.629 Å, resulting in the elongated lattice parameters. Such elongated lattice parameters by K doping are also resolved in the calculated XRD patterns (Figure S5) that are very close to the experimentally recorded XRD patterns. Note that we exclude the formation of K_2Se in the K-doped Cu_2Se. The doped K maintains the form of K^+ cation by replacing Cu^+ cation (Figure S6).

Prior to implementing the K-doped Cu_2Se as a CO_2ER catalyst, we first employ X-ray photoelectron spectroscopy (XPS) to disclose the surface valence states and electronic interplay of Cu, Se and K (Figure S7). The Cu LMM Auger spectra of both $K_{11.2\%}$-Cu_2Se and Cu_2Se show two binding energies at 568.3 and 569.7 eV, corresponding to Cu^{II} and Cu^I, respectively,[10,11] and similar Cu species are also resolved by Cu 2p XPS spectra.[12–14] The Cu^{II} species originates from surface oxidation when exposed to air.[15] In the meantime, K 2p XPS spectrum demonstrates the presence of K^+ in $K_{11.2\%}$-Cu_2Se,[16] suggesting that K^+ cations have been doped into Cu_2Se lattices. This indicates that the incorporation of K^+ cations into Cu_2Se does not notably alter the valence states of the majority of Cu species. However, we observe that the binding energies of Se 3d in $K_{11.2\%}$-Cu_2Se are slightly shifted toward lower values compared to undoped Cu_2Se. This implies that the doped K atoms have transferred electrons to Se atoms due to their electronegativity difference. It is anticipated that this charge

redistribution would alter the electronic structure and behavior of neighbored Cu sites.

Upon recognizing the effect of K doping on tailoring electronic structures, we are in a position to assess the CO_2ER performances of our catalysts. Linear scanning voltammetry (LSV) curves of the catalysts are first measured in 0.1 M $KHCO_3$ electrolyte saturated with Ar or CO_2 (Figure S8). For each catalyst, the onset potential is significantly positively shifted and the current density is substantially raised in CO_2 environment relative to those in Ar environment. This suggests that the catalysts can competently catalyze CO_2ER rather than HER. The K-doped Cu_2Se catalysts display higher current densities than undoped Cu_2Se as the potential becomes more negative than −0.3 V in CO_2-saturated electrolyte. Among the catalysts with various K doping levels, $K_{11.2\%}$-Cu_2Se exhibits the highest current density at the same potential, which turns out to be 97.6 mA cm^{-2} at −1.3 V.

According to the LSV plots, applied potential measurements are carried out from −0.4 to −1.2 V. In all the cases of K-doped Cu_2Se and Cu_2Se, ethanol is the only liquid product detected by ^{1}H nuclear magnetic resonance (NMR) spectroscopy (Figure S9), while CO and H_2 are found in gaseous products by gas chromatography (GC) (Figure S10). As expected, the Faradaic efficiencies of ethanol ($FE_{C_2H_5OH}$) by K-doped Cu_2Se are dramatically higher than those on Cu_2Se at the same potential. Remarkably, $K_{11.2\%}$-Cu_2Se offers the highest $FEs_{C_2H_5OH}$ among different K doping levels (Figure 2a). As displayed in Figure 2b, the $FE_{C_2H_5OH}$ by $K_{11.2\%}$-Cu_2Se exhibits a volcano relationship with applied potentials, which starts as 39.3 % at −0.4 V, achieves an utmost value of 70.3 % as the potential turns more negative to −0.8 V, and is reduced to 52.0 % as the potential is further increased to −1.2 V. Moreover, the $FE_{C_2H_5OH}$ by $K_{11.2\%}$-Cu_2Se is remained over 50 % in a broad potential range from −0.6 to −1.2 V. In sharp contrast, the maximal $FE_{C_2H_5OH}$ by $K_{5.9\%}$-Cu_2Se, $K_{15.9\%}$-Cu_2Se, and Cu_2Se is 27.7 %, 46.0 % and 16.8 % at −0.8, −0.9 and −1.0 V, respectively. Furthermore, the partial current density of ethanol by $K_{11.2\%}$-Cu_2Se achieves 35.8 mA cm^{-2} at −0.8 V, 8.7-fold that by Cu_2Se (4.1 mA cm^{-2}), and reaches a maximal value of 44.4 mA cm^{-2} at −1.2 V (Figure 2c). This demonstrates that K doping can significantly promote the selectivity and activity of Cu_2Se catalyst toward CO_2ER to ethanol while moderate K doping content of 11.2 % enables the highest catalytic performance. Such a performance, particularly the Faradaic efficiency for ethanol, exceeds the representative Cu-based counterparts in literature (Table S1).

Stability is another important parameter for evaluating the catalyst performance. The time-dependent current density and Faradaic efficiency on Cu_2Se and $K_{11.2\%}$-Cu_2Se are monitored through continuous electrolysis for 12 hours at −0.8 V. The $FE_{C_2H_5OH}$ and current density of Cu_2Se are only retained 67.2 % and 88.4 % after 12 h test, respectively (Figure S11a). Notably, our $K_{11.2\%}$-Cu_2Se maintains 95.3 % $FE_{C_2H_5OH}$ and 97.5 % current density after 12 h operation (Figure S11b), demonstrating its application prospect. This high durability of $K_{11.2\%}$-Cu_2Se is enabled by its stable structure and composition except that a small amount of superficial Cu^I species are reduced to Cu^0 during CO_2ER (Figure S12–S14).[17] As the stability test on $K_{11.2\%}$-Cu_2Se is extended to 130 h, the current density and $FE_{C_2H_5OH}$ individually still remain 97.2 % and 90.1 % of their initial values (Figure 2d), showing its extreme catalytic durability.

To explore the origin of enhanced CO_2ER by K doping, we first examine the effect of K doping on active sites and charge transfer dynamics. As displayed in Figure S15, moderate K doping content (11.2 %) can provide maximum electrochemical active surface area (ECSA), boosting contact interface with electrolyte and increasing adsorption sites for various intermediates. After normalized to ECSA, $K_{11.2\%}$-Cu_2Se still shows the largest partial current density for C_2H_5OH in CO_2ER among the catalysts, corroborating its excellent intrinsic catalytic activity. As the CO_2ER process can be promoted by stabilizing $*CO_2^{\bullet-}$ intermediate, the binding strength of OH^- on the catalyst surface is measured given its positive correlation with $*CO_2^{\bullet-}$.[18] It turns out that $*CO_2^{\bullet-}$ intermediate can be effectively stabilized on $K_{11.2\%}$-Cu_2Se (Figure S16a), which would favor its further evolution to other intermediates for ethanol production. Moreover, our electrochemical and optical measurements manifest that K doping can facilitate charge transfer dynamics between the electrode/electrolyte interface and enhance π-electrons delocalization (Figure S16b–d),[19–21] promoting the CO_2ER process.

To further gain information how K dopant participates in the CO_2ER process, time-dependent in situ diffuse reflectance infrared Fourier transform spectroscopy (DRIFTS) is employed to examine the reaction pathway for ethanol production. The DRIFTS spectra on Cu_2Se and $K_{11.2\%}$-Cu_2Se at −0.8 V are collected to disclose the possible reaction intermediates during CO_2ER. In the case of Cu_2Se, the DRIFTS spectra display five bands at 2096, 1704, 1583, 1474 and 1318 cm^{-1} after 2 min of CO_2ER (Figure 3a). The

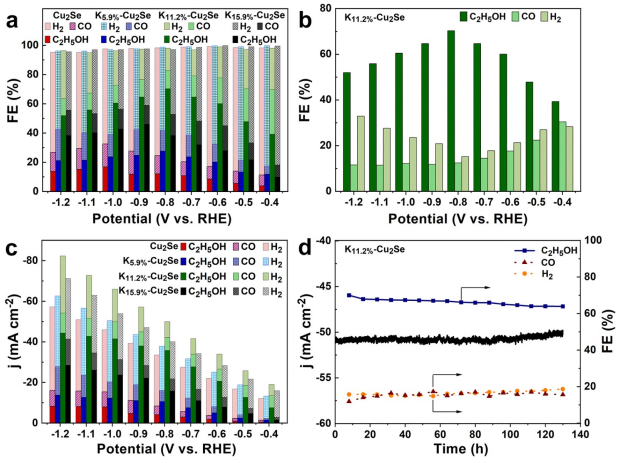

Figure 2. a) Comparison of CO_2ER FEs for K-doped Cu_2Se with various K content and undoped Cu_2Se. b) FEs of ethanol, CO and H_2 for $K_{11.2\%}$-Cu_2Se at different potentials. c) Partial current densities of C_2H_5OH, CO and H_2 from −0.4 to −1.2 V for K-doped Cu_2Se with various K content and undoped Cu_2Se for 2 h. d) Chronopotentiometry test and the corresponding FEs of C_2H_5OH, CO and H_2 for $K_{11.2\%}$-Cu_2Se at −0.8 V for 130 h.

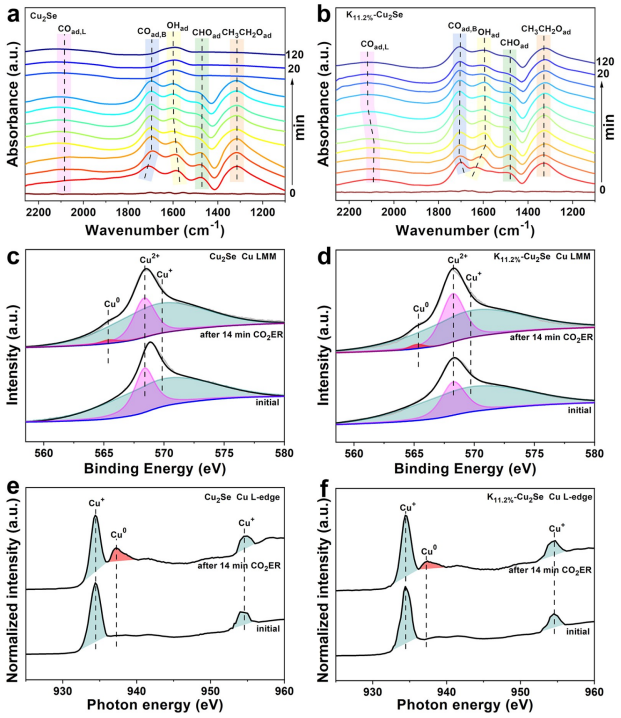

Figure 3. Time-dependent in situ DRIFTS spectra for CO_2ER on a) undoped Cu_2Se and b) $K_{11.2\%}$-Cu_2Se at −0.8 V. Cu LMM Auger spectra of c) Cu_2Se and d) $K_{11.2\%}$-Cu_2Se before and after 14 min CO_2ER at −0.8 V. Cu L-edge XAS spectra of e) Cu_2Se and f) $K_{11.2\%}$-Cu_2Se before and after CO_2ER.

first two peaks are assigned to C=O stretching vibrations of linear $*CO_L$ and bridge $*CO_B$, respectively,[22] while the third peak originates from O–H bending vibration of water molecule,[23] and the last two peaks are ascribed to C=O stretching vibration of *CHO and C–H bending vibration of CH_3CH_2O*, respectively.[22] As the reaction proceeds to 4 min, the peak for $*CO_B$ is shifted to lower wavenumber of 1692 cm^{-1}, which then remains constant until 16 min. On the contrary, the peak for *OH is gradually shifted toward higher wavenumber of 1596 cm^{-1} as the time increases to 10 min, and then remains almost unchanged. $*CO_B$, *CHO and CH_3CH_2O* intermediates disappear as the time is prolonged to 18 min. Such a significant evolution of adsorbed intermediates during the CO_2ER should be ascribed to the further reduction of Cu^I to Cu^0 (Figure S17). It is worth pointing out that the blueshift of *OH peak and the redshift of $*CO_B$ peak with prolonged time at initial reaction stage on Cu_2Se demonstrate the enhanced adsorption of *OH and the weakened adsorption of $*CO_B$ on the catalyst surface, which inevitably boost HER and suppress CO_2ER, respectively.[22]

In comparison, $K_{11.2\%}$-Cu_2Se exhibits very different behavior (Figure 3b). The peak for $*CO_L$ intermediate gradually moves from 2084 cm^{-1} at 8 min to 2110 cm^{-1} at 14 min, and then barely changes. In the meantime, the peak for $*CO_B$ is shifted from 1698 cm^{-1} at 2 min to higher wavenumber of 1708 cm^{-1} at 4 min, after which it remains constant. Contrarily, the peak for *OH is shifted from 1627 cm^{-1} at 2 min toward lower wavenumber of 1589 cm^{-1} as the time increases to 6 min, and then remains almost unchanged. The blueshifts of $*CO_L$ and $*CO_B$ as well as the redshift of *OH on $K_{11.2\%}$-Cu_2Se with extended time at initial reaction stage suggest the strengthened adsorption of $*CO_L$ and $*CO_B$ as well as the attenuated adsorption of *OH on the catalyst surface, which can promote CO_2ER and suppress HER toward our ultimate goal, respectively.[22] After 2 hours of electrolysis, only two intermediates of $*CO_L$ and *OH can be detected on Cu_2Se, while all the intermediates are maintained on $K_{11.2\%}$-Cu_2Se, elucidating that K doping endows the longer residence time of carbonaceous intermediates on the catalyst surface, which contributes to C–C coupling for ethanol production. It has been reported that the synergy of $*CO_L$ and $*CO_B$ can facilitate C–C coupling.[24] As such, the intermediate evolution tuned by K doping eventually enables the highly selective production of ethanol in CO_2ER.

The information gleaned above has resolved the different behavior of intermediates on K-doped and undoped catalysts. We further look into the Cu active sites affected by K dopant. The Cu LMM Auger spectra of Cu_2Se and $K_{11.2\%}$-Cu_2Se are measured to reveal whether the valence states of Cu are changed after 14 min CO_2ER. It turns out that Cu^0 peak appears on Cu_2Se with the peak area ratio of Cu^I to Cu^0 being 1:0.0314 (Figure 3c), while only a small amount of Cu^0 appears on $K_{11.2\%}$-Cu_2Se with the peak area ratio of Cu^I to Cu^0 being 1:0.0198 (Figure 3d).[25–27] Cu L-edge X-ray absorption spectroscopy (XAS) characterization further proves that the valence state of Cu on $K_{11.2\%}$-Cu_2Se makes smaller change after 14 min CO_2ER (Figure 3e and 3f). The signals at 934.4 and 954.5 eV are assigned to Cu^I feature. A new peak at 937.4 eV after 14 min CO_2ER is attributed to Cu^0.[11,24] The ratio of Cu^0 to Cu^I on $K_{11.2\%}$-Cu_2Se is substantially smaller than that on Cu_2Se, which is consistent with the result of Cu LMM Auger spectra. This corroborates the better protection of Cu^I species by K doping. The stabilization of Cu^I sites is critical to the strong adsorption of *CO intermediates, which in turn greatly promotes the C–C coupling in CO_2ER.[28,29]

The in situ DRIFTS spectra on $K_{11.2\%}$-Cu_2Se at different potentials are further carried out to reveal the difference of the reaction intermediates during CO_2ER (Figure S18). The peak for $*CO_L$ intermediate is gradually blue-shifted from 2067 cm^{-1} at −0.4 V to 2110 cm^{-1} at −0.8 V, and then gradually red-shifted toward lower wavenumber of 2054 cm^{-1} as potential negatively moves to −1.2 V. In the meantime, the peak for *OH intermediate is gradually red-shifted from 1654 cm^{-1} at −0.4 V to 1589 cm^{-1} at −0.8 V, and then blue-shifted toward higher wavenumber of 1626 cm^{-1} as potential moves to −1.2 V. The signals for $*CO_B$, *CHO and CH_3CH_2O* intermediates remain largely unchanged as potential varies from −0.4 to −1.2 V. According to the literature,[22] such blueshift of $*CO_L$ peak and redshift of *OH peak on $K_{11.2\%}$-Cu_2Se from −0.4 to −0.8 V well illustrate the boosted CO_2ER and suppressed HER, respectively, whereas the redshift of $*CO_L$ peak and blueshift of *OH peak from −0.8 to −1.2 V demonstrate the other trend. This finding based on intermediate evolution is

consistent with the volcano relationship of Faradaic efficiencies of ethanol and hydrogen with the potential (Figure 2b). Moreover, the intermediate evolution can be well correlated with the valence states of Cu sites. After 14 min of CO_2ER at −0.4 V, the Cu LMM Auger spectrum of $K_{11.2\%}$-Cu_2Se shows no Cu^0 generation (Figure S19). In contrast, Cu^0 peak appears at −1.2 V, in which the peak area ratio of Cu^I to Cu^0 is 1:0.150, significantly higher than that operated at −0.8 V (1:0.0198). This indicates that Cu^I sites are indispensable for C–C coupling in CO_2ER, promoting the production of ethanol at −0.8 V. Note that at −0.4 V, the provided energy is not high enough to generate sufficient intermediates, resulting in the low selectivity of ethanol; however, we can still observe the formation of $*CO_L$ and $*CO_B$ toward ethanol in the absence of Cu^0, excluding the necessity of Cu^0 sites to ethanol production. Taken together, the findings above demonstrate that Cu^I rather than Cu^0 is the key to the success in high ethanol selectivity in our case.

To gain more fundamental insights, DFT calculation is performed for disclosing the origin of K-doped Cu_2Se performance toward CO_2ER to ethanol at atomic levels. The experimentally observed (110) planes are modeled to investigate the reaction mechanism. The theoretical models (Figure S20 and S21) and computational details are provided in Supporting Information. We first analyze the electronic structures of the Cu_2Se (110) and K-doped Cu_2Se (110) planes. The plots of d-projected density of states (d-PDOS) of the surface Cu atoms show the d-band center is upshifted from −2.08 to −1.62 eV by K doping, suggestive of the enhanced reactivity of surface Cu atoms (Figure S22). The whole catalytic mechanisms for CO_2ER into various products (e.g., CO, methanol, methane, ethylene and ethanol) are further explored. Based on the most stable intermediates on Cu_2Se and K-doped Cu_2Se (Figure S23 and S24), the thermodynamically favored pathways with optimized intermediate structures can be obtained (Figure S25–S28).

The calculation reveals that for CO production, the rate-limiting step is the activation of CO_2 by coupling a proton and an electron to yield *COOH on catalyst surface, where the reaction energy is 0.91 eV on Cu_2Se and 0.89 eV on K-doped Cu_2Se, respectively. Afterward, C–O bond of *COOH splits to generate CO, in which the reaction energy is −0.78 eV on Cu_2Se and −0.83 eV on K-doped Cu_2Se, respectively. The free energy profiles (Figure S29) suggest that the K-doped Cu_2Se surface favors both *COOH formation and C–O bond breaking processes. The initial hydrogenation of *CO prefers to generate *CHO rather than *COH with uphill energy of 1.03 eV on Cu_2Se and 0.99 eV on K-doped Cu_2Se (Figure S30), which are both higher than that of *CO desorption (0.58 eV on Cu_2Se, and 0.66 eV on K-Cu_2Se). This explains why CO is the major C_1 product experimentally observed for Cu_2Se and K-doped Cu_2Se catalysts, whereas CO production is quite limited for K-doped Cu_2Se catalyst.

For the C_2 production process, at the low coverage of *CO, stable $*CO_B$ is a dominant adsorption configuration on surface, and *CHO is generated from hydrogenation of $*CO_B$. As *CO coverage increases, it adopts the adsorption form of $*CO_L$ on the neighboring Cu site of *CHO for C–C coupling. $*CO_L$ adsorption energy is 0.14 eV on K-doped Cu_2Se, lower than 0.50 eV on Cu_2Se, indicating the enhanced adsorption of $*CO_L$ around *CHO on K-doped Cu_2Se. The subsequent C–C coupling of *CHO and $*CO_L$ produces *COCHO*, which is endothermic by −0.05 eV on Cu_2Se and −0.02 eV on K-doped Cu_2Se, respectively. Afterward, the sequential hydrogenation of *COCHO* generates *OHCCHO*, *CHO*HCHO and CH_2OHCHO*. Breaking the first C–O bond of CH_2OHCHO* will produce $*CH_2CHO$* with the downhill reaction energies of −0.95 eV on Cu_2Se and −0.73 eV on K-doped Cu_2Se, respectively. Adding hydrogen to $*CH_2CHO$* may produce C_2H_4 (0.96 eV on Cu_2Se, and 0.74 eV on K-doped Cu_2Se), which however is dramatically more difficult than the formation of CH_3C*HO* on surface (−0.07 eV on Cu_2Se, and −0.30 eV on K-doped Cu_2Se), clearly demonstrating that ethylene is scarcely formed. Finally, the stable CH_3CH_2O* is formed on surface, which has been experimentally identified by our in situ DRIFTS spectroscopy. Consequently, the whole reaction mechanism from CO_2 to ethanol is proposed as follows: $2CO_2 \rightarrow 2*COOH \rightarrow *CO_B + *CO_L \rightarrow *CHO + *CO_L \rightarrow$ *COCHO* → *OHCCHO* → *CHO*HCHO → CH_2OHCHO* → $*CH_2CHO$* → CH_3C*HO* → CH_3CH_2O* → C_2H_5O*H → C_2H_5OH (Figure 4a), in which the structures of key intermediates are presented in Figure 4b. The competing HER is

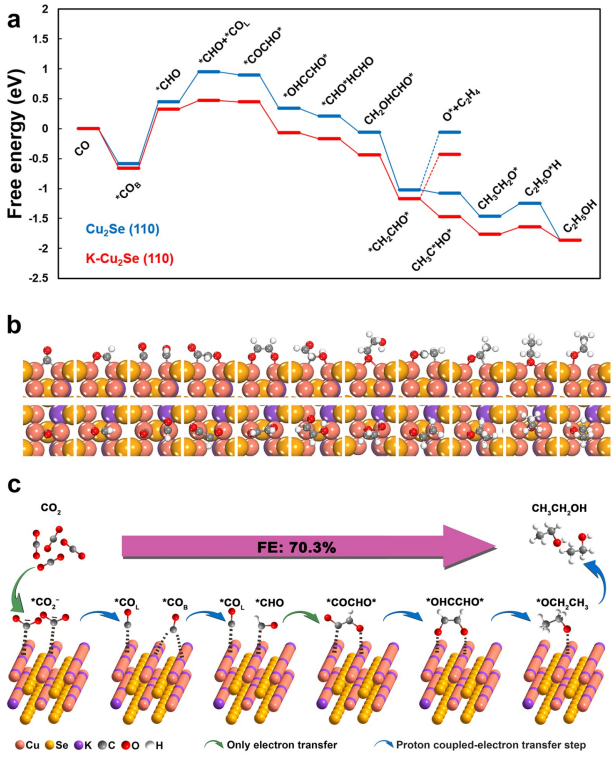

Figure 4. a) Gibbs free energy profiles for the dimerization of *CO to ethylene and ethanol on Cu_2Se (110) (in blue) and K-doped Cu_2Se (110) (in red) planes. b) Top and side views of optimized structures for intermediates on K-doped Cu_2Se (110) during the dimerization of CO to ethylene and ethanol. Cu: orange, Se: yellow, K: purple, C: grey, H: white, O: red. c) Schematic illustration for the catalytic mechanism for ethanol production in CO_2ER on K-doped Cu_2Se.

also considered during CO_2 reduction. Figure S31 shows that K-doped Cu_2Se can suppress the competing HER by the increase of *H binding energy from 0.19 to 0.24 eV, which also helps explain the enhanced Faradaic efficiency of ethanol on K-doped Cu_2Se.

We note that at high-potential conditions, the surface Se may be reduced to H_2Se into electrolyte, leaving Cu^0 sites on surface (Figure S21). The equilibrium potential is calculated to be −1.12 V (vs. RHE), indicating that a small number of Cu^0 sites would exist on surface at low-potential conditions. To evaluate the effect of Cu^0 sites on CO_2ER, we have also calculated the whole catalytic mechanisms of CO_2ER into various products on the reduced Cu_2Se and K-Cu_2Se (Figure S32–S37). It turns out that the C–C coupling still occurs between *CHO and *CO to generate *COCHO* for the C_2 production process (Figure S38); however, the presence of Cu^0 sites makes difference in activity and selectivity. We observe that the formation energy of *COOH from CO_2 is only 0.27 eV on reduced Cu_2Se and 0.20 eV on reduced K-Cu_2Se, significantly lower than 0.91 eV on Cu_2Se and 0.89 eV on K-doped Cu_2Se (Figure S39), facilitating the formation of *CO. The activation of *CO to produce *CHO is also promoted (Figure S40). Although it seems that the Cu^0 sites can benefit CO_2ER, the HER is also dramatically enhanced, resulting a product selectivity issue. Figure S41 shows that the H* binding energies are −0.05 eV on reduced Cu_2Se and 0.02 eV on reduced K-Cu_2Se, respectively (−0.07 eV on Cu_2Se, and −0.30 eV on K-doped Cu_2Se), indicating rather high hydrogen evolution activity in the presence of Cu^0 sites. This enhancement of HER by Cu^0 sites is particularly notable in the case of K-doped catalyst, suggesting that preventing the reduction of Cu^I to Cu^0 is very necessary for high selectivity.

According to the results of in situ DRIFTS spectra, Cu LMM Auger spectra and Cu L-edge XAS spectra of $K_{11.2\%}$-Cu_2Se and Cu_2Se combined with DFT calculation, the catalytic mechanism of CO_2ER to ethanol on K-doped Cu_2Se is inferred as follows: the electrons transferred from K atoms to Se atoms in K-doped Cu_2Se promote the C-terminal adsorption of CO_2 molecules on Cu sites,[30] which results in the weakening of C–O bonds of CO_2 molecules. Consequently, this promotes the evolution of linear CO_2 to bent $*CO_2^{\bullet-}$, which is subsequently reduced to linear $*CO_L$ and bridge $*CO_B$ by proton coupled-electron transfer step. According to the literature,[24] the bridge adsorption of $*CO_B$ with negative charge can take place on the Cu sites with positive charge. In our case, the Cu sites near K^+ can play such a role. K doping increases the binding strengths of $*CO_B$ and $*CO_L$, and promotes the hydrogenation of $*CO_B$ to *CHO. Subsequently, *CHO is coupled with $*CO_L$ to generate *COCHO* intermediate, which is adsorbed on two Cu sites with one C-terminal binding and another O-terminal binding. After multiple proton coupled-electron transfer steps, *COCHO* intermediate is converted into CH_3CH_2O* intermediate, which is adsorbed on Cu site with O-terminal binding. The enhanced binding of $*CO_B$ on K-doped Cu_2Se occupies more Cu sites to weaken *OH adsorption, which thus suppresses HER and contributes to CO_2ER. The nanosheets array structure provides profuse active sites for adsorption of CO_2 and various intermediates. The exposure of (220) crystal plane of Cu_2Se benefits the adsorption of $*CO_B$,[31] a key intermediate for C–C coupling, resulting in a handful of ethanol production during CO_2ER on undoped Cu_2Se. Upon K doping, the electronic structure of Cu_2Se is modulated to better protect Cu^I species during CO_2ER, which prolongs the retention time of carbonaceous intermediates, thereby accelerating the rate of CO_2ER to ethanol. Figure 4c displays the overall catalytic mechanism for ethanol production in CO_2ER on K-doped Cu_2Se.

Conclusion

In conclusion, K-doped Cu_2Se nanosheet arrays have been developed on Cu foam for CO_2ER to give ethanol as a single liquid product with high selectivity. The exposed (220) crystal plane endows the adsorption of a key bridge-bonded $*CO_B$ intermediate. The K doping promotes the adsorption of linear $*CO_L$ and bridge $*CO_B$ intermediates on the catalyst surface, enhancing subsequent C–C coupling to produce ethanol. This promotion works through the protection of Cu^I sites by K doping during CO_2ER. As a result, the optimal $K_{11.2\%}$-Cu_2Se nanosheet array can achieve a Faradaic efficiency as high as 70.3 % and a partial current density of 35.8 mA cm^{-2} for ethanol at −0.8 V in 0.1 M $KHCO_3$ with a robust stability for 130 h. Moreover, the Faradaic efficiency of ethanol exceeds 50 % in a broad potential range from −0.6 to −1.2 V, suggesting that the catalyst has a great potential for real application. This work provides a new approach to maneuver the evolution of reaction intermediates to boost CO_2ER to ethanol by alkali-metal doping, and provides a rational strategy for designing catalysts toward multiple proton coupled-electron transfer reactions with high product selectivity.

Acknowledgements

This work was financially supported in part by the National Natural Science Foundation of China (21671006, 21725102, 21901007, 21903001), the Natural Science Foundation of Anhui Province (1908085QB58), Natural Science Research Project for Universities in Anhui Province (KJ2021ZD0006), and the University Synergy Innovation Program of Anhui Province (GXXT-2021-020, GXXT-2020-073, GXXT-2020-074).

Conflict of Interest

The authors declare no conflict of interest.

Data Availability Statement

The data that support the findings of this study are available from the corresponding author upon reasonable request.

Keywords: C–C Coupling · CO_2 Reduction · Doping · Electrocatalysis · Ethanol

[1] K. P. Kuhl, E. R. Cave, D. N. Abram, T. F. Jaramillo, *Energy Environ. Sci.* **2012**, *5*, 7050–7059.
[2] H. Xu, Y. Ma, J. Chen, W. Zhang, J. Yang, *Chem. Soc. Rev.* **2022**, *51*, 2710–2758.
[3] S. H. Lee, J. C. Lin, M. Farmand, A. T. Landers, J. T. Feaster, J. E. Aviles Acosta, J. W. Beeman, Y. Ye, J. Yano, A. Mehta, R. C. Davis, T. F. Jaramillo, C. Hahn, W. S. Drisdell, *J. Am. Chem. Soc.* **2021**, *143*, 588–592.
[4] X. Wang, Z. Wang, F. P. G. de Arquer, C. T. Dinh, A. Ozden, Y. C. Li, D. H. Nam, J. Li, Y. S. Liu, J. Wicks, Z. Chen, M. Chi, B. Chen, Y. Wang, J. Tam, J. Y. Howe, A. Proppe, P. Todorović, F. Li, T. T. Zhuang, C. M. Gabardo, A. R. Kirmani, C. McCallum, S. F. Hung, Y. Lum, M. Luo, Y. Min, A. Xu, C. P. O'Brien, B. Stephen, B. Sun, A. H. Ip, L. J. Richter, S. O. Kelley, D. Sinton, E. H. Sargent, *Nat. Energy* **2020**, *5*, 478–486.
[5] F. Li, Y. C. Li, Z. Wang, J. Li, D. H. Nam, Y. Lum, M. Luo, X. Wang, A. Ozden, S. F. Hung, B. Chen, Y. Wang, J. Wicks, Y. Xu, Y. Li, C. M. Gabardo, C. T. Dinh, Y. Wang, T. T. Zhuang, D. Sinton, E. H. Sargent, *Nat. Catal.* **2020**, *3*, 75–82.
[6] P. P. Yang, X. L. Zhang, F. Y. Gao, Y. R. Zheng, Z. Z. Niu, X. Yu, R. Liu, Z. Z. Wu, S. Qin, L. P. Chi, Y. Duan, T. Ma, X. S. Zheng, J. F. Zhu, H. J. Wang, M. R. Gao, S. H. Yu, *J. Am. Chem. Soc.* **2020**, *142*, 6400–6408.
[7] T. T. Zhuang, Z. Q. Liang, A. Seifitokaldani, Y. Li, P. De Luna, T. Burdyny, F. Che, F. Meng, Y. Min, R. Q. Bermudez, C. T. Dinh, Y. Pang, M. Zhong, B. Zhang, J. Li, P. N. Chen, X. L. Zheng, H. Liang, W. N. Ge, B. J. Ye, D. Sinton, S. H. Yu, E. H. Sargent, *Nat. Catal.* **2018**, *1*, 421–428.
[8] D. Yang, Q. Zhu, C. Chen, H. Liu, Z. Liu, Z. Zhao, X. Zhang, S. Liu, B. Han, *Nat. Commun.* **2019**, *10*, 677.
[9] Y. Y. Mi, X. Y. Peng, X. J. Liu, J. Luo, *ACS Appl. Energy Mater.* **2018**, *1*, 5119–5123.
[10] X. Qian, L. Zhang, Y. Lin, M. Wang, X. Wang, W. Su, *Appl. Surf. Sci.* **2021**, *568*, 150985.
[11] H. Jung, S. Y. Lee, C. W. Lee, M. K. Cho, D. H. Won, C. Kim, H. S. Oh, B. K. Min, Y. J. Hwang, *J. Am. Chem. Soc.* **2019**, *141*, 4624–4633.
[12] J. Masud, W. P. R. Liyanage, X. Cao, A. Saxena, M. Nath, *ACS Appl. Energy Mater.* **2018**, *1*, 4075–4083.
[13] C. Wei, D. Zhong, D. Li, G. Hao, G. Liu, J. Li, Q. Zhao, *Int. J. Hydrogen Energy* **2019**, *44*, 31979–31986.
[14] Y. Li, X. Sun, Z. Cheng, X. Xu, J. Pan, X. Yang, F. Tian, Y. Li, J. Yang, Y. Qian, *Energy Storage Mater.* **2019**, *22*, 275–283.
[15] S. C. Riha, D. C. Johnson, A. L. Prieto, *J. Am. Chem. Soc.* **2011**, *133*, 1383–1390.
[16] L. Lin, W. Ren, C. Wang, A. M. Asiri, J. Zhang, X. Wang, *Appl. Catal. B* **2018**, *231*, 234–241.
[17] J.-Y. Park, Y.-S. Jung, J. Cho, W.-K. Choi, *Appl. Surf. Sci.* **2006**, *252*, 5877–5891.
[18] F. Lei, W. Liu, Y. Sun, J. Xu, K. Liu, L. Liang, T. Yao, B. Pan, S. Wei, Y. Xie, *Nat. Commun.* **2016**, *7*, 12697.
[19] B. D. Yang, J. Yang, Z. Huang, L. Z. Qin, H. Lin, Q. Li, *Appl. Surf. Sci.* **2021**, *535*, 147712.
[20] G. Sığırcık, T. Tüken, *Mater. Sci.: Mater. Electron.* **2020**, *31*, 17855–17871.
[21] S. Wang, J. Zhan, K. Chen, A. Ali, L. Zeng, H. Zhao, W. Hu, L. Zhu, X. Xu, *ACS Sustainable Chem. Eng.* **2020**, *8*, 8214–8222.
[22] Y. Katayama, F. Nattino, L. Giordano, J. Hwang, R. R. Rao, O. Andreussi, N. Marzari, Y. Shao-Horn, *J. Phys. Chem. C* **2019**, *123*, 5951–5963.
[23] E. Pérez-Gallent, M. C. Figueiredo, F. Calle-Vallejo, M. T. M. Koper, *Angew. Chem. Int. Ed.* **2017**, *56*, 3621–3624; *Angew. Chem.* **2017**, *129*, 3675–3678.
[24] T.-C. Chou, C.-C. Chang, H.-L. Yu, W.-Y. Yu, C.-L. Dong, J.-J. Velasco-Velez, C.-H. Chuang, L.-C. Chen, J.-F. Lee, J.-M. Chen, H.-L. Wu, *J. Am. Chem. Soc.* **2020**, *142*, 2857–2867.
[25] C. Peng, Z. Xu, G. Luo, S. Yan, J. Zhang, S. Li, Y. Chen, L. Y. Chang, Z. Wang, T.-K. Sham, G. Zheng, *Adv. Energy Mater.* **2022**, *12*, 2200195.
[26] I. Platzman, R. Brener, H. Haick, R. Tannenbaum, *J. Phys. Chem. C* **2008**, *112*, 1101–1108.
[27] C. Guo, Y. Guo, Y. Shi, X. Lan, Y. Wang, Y. Yu, B. Zhang, *Angew. Chem. Int. Ed.* **2022**, *61*, e202205909; *Angew. Chem.* **2022**, *134*, e202205909.
[28] X. Yuan, S. Chen, D. Cheng, L. Li, W. Zhu, D. Zhong, Z. J. Zhao, J. Li, T. Wang, J. Gong, *Angew. Chem. Int. Ed.* **2021**, *60*, 15344–15347; *Angew. Chem.* **2021**, *133*, 15472–15475.
[29] M. Li, Y. Ma, J. Chen, R. Lawrence, W. Luo, M. Sacchi, W. Jiang, J. Yang, *Angew. Chem. Int. Ed.* **2021**, *60*, 11487–11493; *Angew. Chem.* **2021**, *133*, 11588–11594.
[30] A. Saxena, W. Liyanage, J. Masud, S. Kapila, M. Nath, *J. Mater. Chem. A* **2021**, *9*, 7150–7161.
[31] J. Y. Kim, G. Kim, H. Won, I. Gereige, W. B. Jung, H. T. Jung, *Adv. Mater.* **2022**, *34*, 2106028.

Manuscript received: June 24, 2022
Accepted manuscript online: July 14, 2022
Version of record online: July 28, 2022